Progress In Electromagnetics Research, Vol. 128, 137–151, 2012

PERFORMANCE ANALYSIS OF THE SCENARIO-BASED CONSTRUCTION METHOD FOR REAL TARGET ISAR RECOGNITION

S.-H. Park[1], J.-H. Lee[2], and K.-T. Kim[3,*]

[1]Department of Electronic Engineering, Pukyong National University, Busan, Korea

[2]Department of Information and Communication Engineering, Sejong University, Seoul, Korea

[3]Department of Electronic Engineering, Pohang University of Science and Technology, Pohang, Korea

Abstract—Due to the difficulty in estimating the 2D image plane of the inverse synthetic aperture radar (ISAR) image, we recently proposed a new paradigm to construct the training database based on the flight scenario. However, because the flight condition for the training and the test data was identical, much more study is required for this method to be applied to the real ISAR scenario. This paper presents a study on the factor that can affect the applicability of scenario-based method to the real target ISAR recognition. Simulation results using five scatterer models show that accurate measurement of flight direction and aspect angle variation are required and enough bandwidth larger than 200 MHz should be guaranteed for the successful classification.

1. INTRODUCTION

Inverse Synthetic Aperture Radar (ISAR) imaging is a technique applied to generate a high resolution two-dimensional (2D) image of a target [1–8] and shows the 2D distribution of the radar prospection (RCS) [9–17] of the target. This image can be generated by synthesizing many range profiles [18, 19] obtained from various observation angles. In this process, the scattering centers of a target are projected onto the 2D image plane formed by the rotational component of the target. ISAR has many military applications [20].

Received 22 March 2012, Accepted 15 May 2012, Scheduled 23 May 2012

* Corresponding author: Kyung-Tae Kim (kkt@postech.ac.kr).

Because of the 2D nature of the ISAR image, construction of the training database for automated recognition requires estimation of 2D image plane of a target. This requirement impedes successful recognition because, in reality, targets are generally engaged in complicated motions, which seriously degrade the classification result if image planes corresponding to such motions are not correctly measured during the training phase. For this reason, we have previously proposed a new paradigm in which a training database was constructed based on the flight scenarios of the target to compare the test image of the target with the training image that corresponds to the flight scenario of the unknown target [21].

Although our simulations have proved the efficiency of the new paradigm under the ideal condition that used five point scatterer models modeled by applying the computer aided design CAD data of the real aircraft, the new paradigm still needs to be studied further before it can be applied to the real target recognition. In the real measurement scenario, discrepancy between the training database and the test database can occur due to the differences in the flight direction $\vec{v}_d$ and the aspect angle variation $\Delta\theta$ of the target. In addition, the limitation on the available bandwidth can degrade the performance of the scenario-based paradigm.

This paper conducts an in-depth analysis of the scenario-based training-database construction method in terms of signal-to-noise ratio, bandwidth, training data size and the classification method under the error in the flight direction and the aspect angle variation. In simulations using five scatterer models, accurate measurements of $\vec{v}_d$ and $\Delta\theta$, bandwidth $B \geq 200\,\text{MHz}$ were required for successful recognition. When $\vec{v}_d$ was at an angle to the viewing vector, the size of the training data could be reduced to 21.7% of the original size.

2. PRINCIPLES OF THE SCENARIO-BASED CONSTRUCTION METHOD

2.1. The Scenario-based Construction Method

Because infinite memory space and classification time would be required to store 2D training images for all rotational angles at each 3D point, we proposed a scenario-based construction method [21]. In this method, the 3D space (training space) was uniformly sampled assuming that a target moved at a given velocity in a given direction vector, $\vec{v}_d$, starting from each given grid point. Then, after deriving angular variation $\Delta\theta$ that yields the same cross-range resolution $\Delta r_c = \lambda/(2\Delta\theta)$ (λ = wavelength) as the range resolution Δr, the image was stored in the training database (Fig. 1).

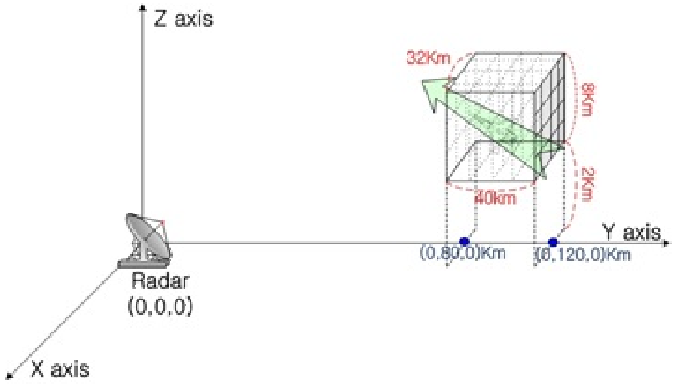

Figure 1. Scenario-based construction method.

In deriving the ISAR image, we avoided the time-consuming translational motion compensation using completely known motion parameters of the target. Using the known azimuth angle ϕ and elevation angle θ at each pulse emission, the aircraft pose was constructed by rotating the target around the z and y axes. Then, the received radar signal was computed and the ISAR image was obtained by using matched-filtering in the range direction and inverse Fourier transform (IFT) in the cross-range direction.

2.2. Signal Modeling and Imaging Algorithm

For the radar signal, we assume the monostatic chirp radar signal widely used for high resolution radar imaging. The transmitted chirp signal is given by

$$r(t) = A_0 e^{j2\pi\left(f_0 t + \frac{Bt^2}{2\tau}\right)} \times rect\left(\frac{t}{\tau}\right) \tag{1}$$

where $r(t)$ is a transmitted signal at time t, A_0 is its amplitude, f_0 is the start frequency, B is the bandwidth, τ is the pulse duration and $rect$ is a function whose value is 1 for $t - \tau/2 \leq t \leq t + \tau/2$ and 0 otherwise. The received signal reflected from a target composed of K scattering centers at aspect angle θ is

$$g(\theta, t) = \sum_{k=1}^{K} A_k e^{j2\pi\left(f_0(t-d_{k,\theta}) + \frac{B(t-d_{k,\theta})^2}{2\tau}\right)} \times rect\left(\frac{t - d_{k,\theta}}{\tau}\right) \tag{2}$$

where A_k is the amplitude of scattering center k, and $d_{k,\theta}$ is the time delay between the radar and scattering center k; $d_{k,\theta}$ is calculated using

plane wave approximation, in which the distance to a scattering center is that projected onto the radar line-of-sight vector.

For ISAR imaging, we use the range-Doppler algorithm [22–24], which assumes that the relative rotational angle between the target and the radar is small and scatterers do not migrate into neighboring range bins for the small angle variation. This algorithm consists of four steps: range compression, TMC and azimuth compression. In range compression, the reflected signal (2) is matched-filtered to yield the high resolution range profile (RP) at each aspect angle and TMC is carried out to remove the phase error caused by the motion of the target. Finally, the fast Fourier transform (FFT) is conducted to each range bin to resolve scattering centers in the cross-range direction. Among the three steps, TMC is the most important step and is composed of two steps: range alignment and phase adjustment. One dimensional entropy minimization method was used for the range alignment and for the phase adjustment, two dimensional entropy minimization method was used (see [22–24]).

2.3. Multiple Signal Classification (MUSIC) Algorithm

This paper applies a multiple signal classification (MUSIC) algorithm to further improve the resolution of the ISAR image. This method belongs to the modern spectral estimation technique and is based on the characteristic that the eigen vector of the noise in the covariance matrix is orthogonal to the direction vector of the scatterer on the ISAR image. Once the covariance matrix is estimated, the b eigen vectors corresponding to the smallest b eigen values constitute the noise matrix $\mathbf{E}_n^H$ and the ISAR image is given as

$$I_{\mathrm{MUSIC}}(x,y) = \frac{\mathbf{e}(x,y)^H \mathbf{e}(x,y)}{\mathbf{e}(x,y)^H \mathbf{E}_n^H \mathbf{E}_n \mathbf{e}(x,y)} \tag{3}$$

where $\mathbf{e}\,(x,\ y)$ is the direction vector at $(x,\ y)$ position on the image and H is the complex conjugate transpose. If a scatterer exists at $(x,\ y)$, $\mathbf{e}\,(x,\ y)$ is orthogonal to $\mathbf{E}_n^H$ and the denominator in (3) becomes 0 or very close to 0. Therefore, a sharp peak is generated at that position. MUSIC is used to derive high resolution ISAR images using narrow-band radar signals (see [5] for the procedure).

2.4. Classification Method and Overall Classification Procedure

Two classifiers are compared in this paper; the nearest neighbor classifier (NNC) using the principal component analysis (PCA) [25–27] of the image classifier and the polar mapping classifier (PMC). For

the NNC, each $M \times N$ training image k is first aligned using the center of mass (COM) of the first image which is converted to $MN \times 1$ vector $\mathbf{f}_k$. Then, PCA is applied to reduce the dimension of the vector and to remove the redundancy in the vector. $\mathbf{f}_k$ is compressed into a feature vector with a smaller dimension l using the PCA matrix $\mathbf{P}$ as follows:

$$\mathbf{x} = \mathbf{P}^T \mathbf{f}_k \tag{4}$$

where

$$\mathbf{P} = [\mathbf{v}_1, \mathbf{v}_2, \ldots, \mathbf{v}_l] \tag{5}$$

The column vector $\mathbf{v}_k$ in $\mathbf{P}$ are the eigen vectors corresponding to the largest l eigen values of the sample covariance matrix [28]. $\mathbf{P}$ is also used to compress the test vector of the aligned test image and the compressed vector is inserted to NNC for the final classification. NNC uses a simple Euclidean distance between two vectors

$$d(\mathbf{x}_1, \mathbf{x}_2) = \|\mathbf{x}_1 - \mathbf{x}_2\| \tag{6}$$

Then, the class of an unknown test vector $\mathbf{x}_u$ is determined by

$$i = \min_i d(\mathbf{x}_u, \mathbf{x}_i) \tag{7}$$

where $\mathbf{x}_i$ is a training vector compressed by PCA that belongs to the target i.

The PMC [28] used in this paper is invariant to the variation of the scale, and the translation of the ISAR image uses a projection of the polar mapped image onto the r-axis (r-projected image), a projection onto the θ-axis (θ-projected image), and the polar image compressed by PCA. Targets in the training database are coarsely sifted using the correlation coefficients of their r-projected images, and the θ-projected images of the coarsely-sifted targets are fine-sifted by seeking the maximum cross-correlation. The final decision is made using the PCA images of the fine-sifted images.

Based on the principles mentioned above, classification is conducted using the unknown target. The test target starts from a random location in the training space, and the reflected signal is collected at each point on the trajectory. Then, matched-filtering, TMC and cross-range FFT are applied to obtain the test ISAR image (Fig. 2), and the absolute value of the derived image is used for classification using PCA + NNC and PMC. Classification performance is expressed as the correct classification percentage

$$Pc = \frac{N_c}{N_t} \times 100\% \tag{8}$$

where N_c is the number of the correct identifications and N_t is the number of test sets.

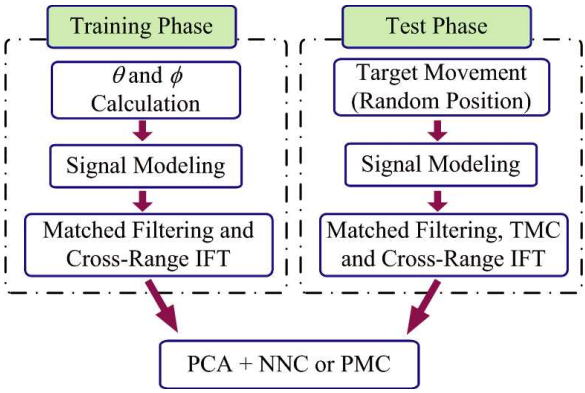

Figure 2. Classification procedure.

3. SIMULATION RESULTS

3.1. Effect of the Errors in the $\vec{v}_d$ and the $\Delta\theta$

The first simulation was conducted to study the effect of the errors in $\vec{v}_d$ and $\Delta\theta$. We used five targets consisting of isotropic point scatterers derived from 3D CAD data of real aircraft; Boeing 737, F18, F14, Su35, and Rafale jets (www.3dcadbrowser.com). As in the general ISAR simulation, jet engine modulation [29–32] was not considered. For the radar system, we used a monostatic chirp radar with pulse repetition frequency = 2 kHz, center frequency = 9.15 GHz, B = 200 MHz (cross-range resolution Δr_c = 0.75 m), sampling frequency = 512 MHz and τ = 30 µs. To study the effect of the noise, reflected signals were collected with the signal-to-noise ratios (SNRs) 0, 10, 20 and 30 dB.

To construct the training images, we assumed that the jets were flying at velocity v = 300 m/s in one of three directions, $\vec{v}_d = [0\ -1\ 0]$, $[-1\ -1\ 0]$ and $[-1\ 0\ 0]$, until they reach $\Delta\theta = 1.26°$, which corresponds to the cross-range Δr_c. Because the angular variation is large in $\vec{v}_d = [-1\ -1\ 0]$ and $[-1\ 0\ 0]$, the test space for these scenarios was constructed at a long range using axis values $80 \leq y \leq 120$ km, $-16 \leq x \leq 16$ km, and $2 \leq z \leq 10$ km. However, because the angular variation which is mainly due to the elevation variation is very small for $[0\ -1\ 0]$ flight, the range in y-axis was $6 \leq y \leq 10$ km, $-16 \leq x \leq 16$ km and $2 \leq z \leq 10$ km. Then 125 training samples per target were stored by dividing the training space into $5 \times 5 \times 5 = 125$ grid points in each of the three axes ($125 \times 5 = 625$ training images). For each scenario, 50 images of each target were derived ($50 \times 5 = 250$ test images).

In the test phase, two groups of test images were constructed;

one without the errors and the other with the errors in $\vec{v}_d$s and $\Delta\theta$s to include errors in the real measurement situation; error in $\vec{v}_d$ yields different image planes from those in the training database and the error in $\Delta\theta$ cause scaling of the image in cross-range direction. In this paper, the test $\vec{v}_d$ was selected at random in a range of $\pm[0.1\,0.1\,0.1]$ from the training $\vec{v}_d$ and $\Delta\theta$ was selected at random in a range of $1.26 \pm 0.5°$ ($0.534 \leq \Delta r_c \leq 1.235$ m). For the aircraft motion, a range of velocities ($250 \leq v \leq 350$ m/s) and accelerations a ($0 \leq a \leq 5$ m/s^2) were used to consider the difference of v and a between the training and the test targets.

The $\vec{v}_d$s for the test ISAR image were much different from $[0\ -1\ 0]$ due to the error (Fig. 3(a)), and the ISAR images with the $+0.5°$ and $-0.5°$ angle errors at 30 dB SNR were different due to the scaling in cross-range direction (Figs. 3(b) and (c)). In this scenario, scatterers were not well-spread in the two images because the ISAR images were mainly formed using the elevation angle variation and thus, the degree

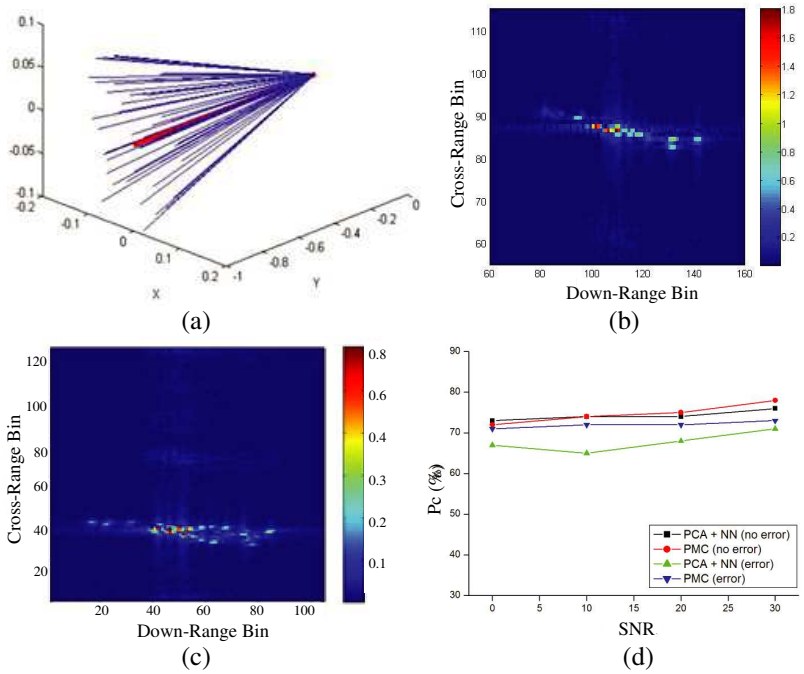

Figure 3. Flight directions, scaled ISAR images and classification result ($\vec{v}_d = [0\ -\ 1\ 0]$). (a) Flight directions. (b) ISAR image ($\Delta\theta = 0.76°$). (c) ISAR image ($\Delta\theta = 1.76°$). (d) Classification result.

of scaling was not considerable. The overall performance of PMC was better than that of PCA + NNC due to the translational and the rotational invariance of the PMC (Fig. 3(d)). For PCA + NNC, the image can be rotationally variant even though it is aligned using COM. This variance degraded the classification result. The performance degradation of PMC (ranging between 1 and 5%) was smaller than that of PCA + NN (ranging between 6 and 9%) in both cases.

In the scenario of $\vec{v}_d = [-1\ -1\ 0]$, scatterers were well-spread in the two images because the ISAR images were mainly formed using the azimuth angle variation (Figs. 4(a) and (b)). Due to the large scale difference, a larger degradation of Pcs was yielded for PMC than that in $[0\ -1\ 0]$; the amount of degradation ranged from 4 to 9% for both PCA + NNC and PMC (Fig. 4(c)). The overall performance of PMC is better than PCA + NNC.

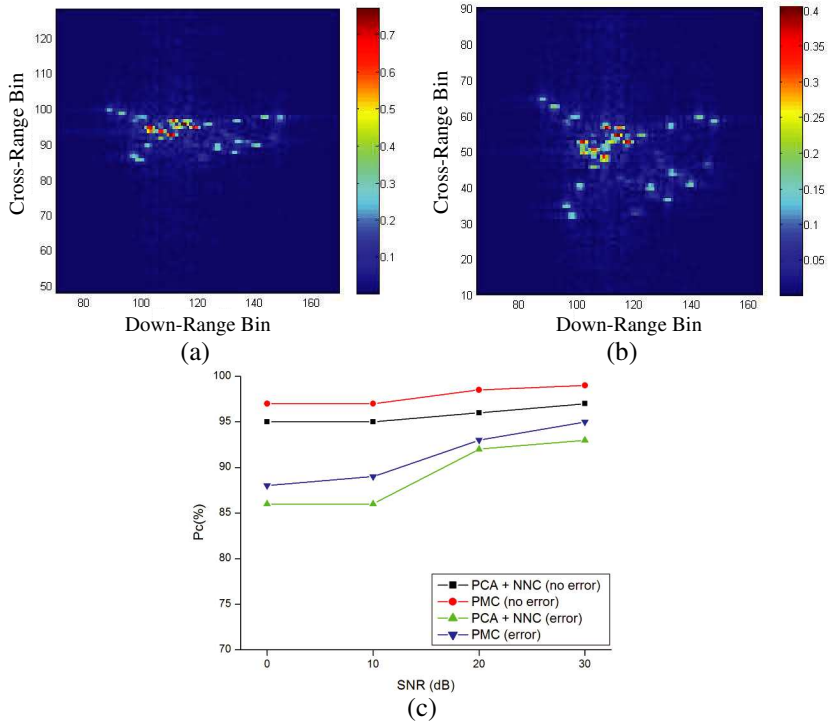

Figure 4. Scaled ISAR images and classification result ($\vec{v}_d = [-1\ -\ 1\ 0]$). (a) ISAR image ($\Delta\theta = 0.76°$). (b) ISAR image ($\Delta\theta = 0.76°$). (c) Classification result.

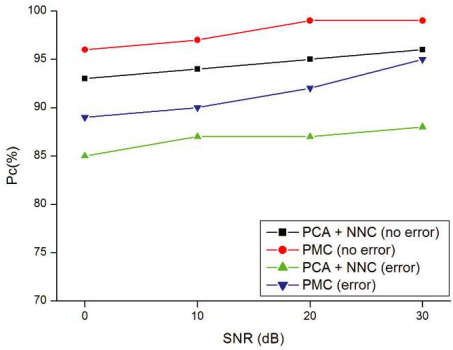

Figure 5. Classification result ($\vec{v}_d = [-1\,0\,0]$).

PMC outperformed PCA + NNC for all SNRs in the scenario of $\vec{v}_d = [0\ -1\,0]$. Similar to the $[-1\ -1\,0]$ direction, the degree of image scaling was larger than that in $[0\ -1\,0]$ direction, and thus, degradation of Pcs in PMC was larger than that in $[0\ -1\,0]$; the amount of degradation ranged from 4 to 9% for both PCA + NNC and PMC (Fig. 5).

3.2. Effect of Bandwidth Reduction

To study the effect of the reduction in B, two Bs, 100 MHz (Δr = 1.5 m) and 200 MHz (Δr = 1.5 m), were used at SNR = 10 dB under the same simulation condition as in the Subsection 3.1. For the two groups of test images mentioned above, the simulation results using PCA + NNC and PMC were compared for each scenario.

For each flight direction, reduction of Pcs was considerable regardless of the error in $\vec{v}_d$ and $\Delta\theta$ (Table 1). Due to the lower quality of the ISAR image, PCA + NNC yielded poor results. In PMC, poor estimation of COM yielded poor r and θ-projected images, and as a result, Pcs decreased. In the first case (without error), the reduction of Pcs in PCA + NNC was 7.6, 20.4, and 18.8% in the three $\vec{v}_d$s. In PMC, the reduction was 20, 21.6 and 11.6%. In the second case (with error), Pcs in PCA + NNC decreased by 8, 19.2 and 14.8% and the reduction of Pcs in PMC was 17.2, 28.8, and 33.2%.

3.3. Result of MUSIC Algorithm

For each $\vec{v}_d$, MUSIC was applied to the training and the test ISAR images were derived at SNR = 10 dB to further improve the resolution,

Table 1. Result of MUSIC.

Scenario	B	PCA + NNC	PMC
$\vec{v}_d = [0\ -1\ 0]$	200 MHz	65.2%	72.0%
	100 MHz	57.2%	54.8%
$\vec{v}_d = [-1\ -1\ 0]$	200 MHz	86.0%	89.2%
	100 MHz	66.8%	60.4%
$\vec{v}_d = [-1\ 0\ 0]$	200 MHz	87.2%	90.4%
	100 MHz	72.4%	57.2%

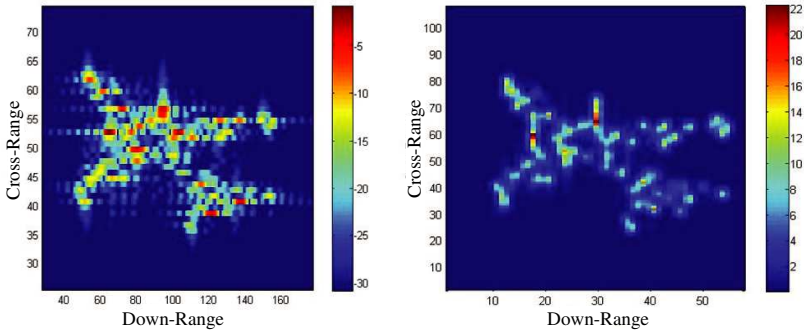

Figure 6. Enhancement of ISAR image by MUSIC at $B = 200$ MHz ($\vec{v}_d = [-1\ -1\ 0]$). (a) Original, (b) MUSIC.

and the performance was compared with that of the original image. Simulation conditions were the same as in Subsection 3.2. The subarray size to derive the covariance matrix for MUSIC was sent to $M/3 \times N/3$ (see [13] for the definition of the subarray). Clearly, the resolution of the ISAR image was improved by MUSIC algorithm (Fig. 6).

At $B = 200$ MHz, MUSIC did not improve Pcs very much; Pcs slightly increased for PCA + NNC and slightly decreased for PMC (Table 2). This proves that $B = 200$ MHz with the conventional range-Doppler algorithm provides high-resolution ISAR images good enough for the recognition of the real-sized jets. At 100 MHz, MUSIC increased Pcs considerably. The amount of improvement in PMC was more than that in PCA because Pcs in PMC decreased very much due to the bandwidth reduction. These findings led us to conclude that time-consuming MUSIC is not necessary if enough bandwidth is given by the radar system.

Table 2. Effect of MUSIC.

Scenario	B	Original image		Image by MUSIC	
		PCA + NNC	PMC	PCA + NNC	PMC
$\vec{v}_d = [0\ -1\ 0]$	200 MHz	65.2%	72.0%	66.8%	69.2%
	100 MHz	57.2%	54.8%	71.2%	67.2%
$\vec{v}_d = [-1\ -1\ 0]$	200 MHz	86.0%	89.2%	87.2%	88.4%
	100 MHz	66.8%	60.4%	78.8%	80.8%
$\vec{v}_d = [-1\ 0\ 0]$	200 MHz	87.2%	90.4%	86.4%	90.8%
	100 MHz	72.4%	57.2%	79.6%	82.4%

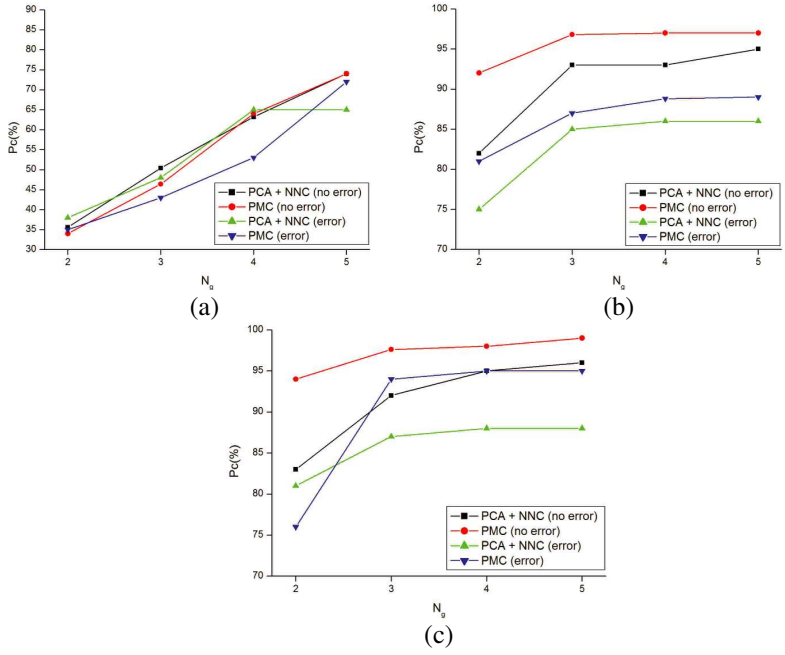

Figure 7. Classification result for training data reduction. (a) $[0\ -1\ 0]$. (b) $[-1\ -1\ 0]$. (c) $[-1\ 0\ 0]$.

3.4. Effect of Training Data Reduction

We also conducted a simulation to study the influence of the number of the training images $N_{tr} = N_g^3$ per target where N_g is the number of grids in each axis. N_g was changed from 5 to 2 at SNR = 10 dB. For $\vec{v}_d = [0\ -1\ 0]$, ISAR images did not represent each target clearly because scatteres were positioned in narrow regions (see Fig. 3).

Therefore, Pcs were very sensitive N_g reduction (Fig. 7(a)). For $\vec{v}_d = [-1\ -1\ 0]$ and $[-1\ 0\ 0]$, ISAR images represented each target very clearly because scatterers were widely spread in the image. Therefore, Pcs for $3 \leq N_g \leq 5$ did not decreased considerably. Because Pcs reduced less than 2% for $N_g = 3$, the training data size could be reduced to $27/125\times = 21.6\%$ of the original training database in the two scenarios (Figs. 7(b) and (c)).

4. CONCLUSION

To enable the scenario-based construction method to recognize targets successfully, this paper performed an in-depth analysis of the scenario-based method to construct an ISAR training database using PCA + NNC and PMC in the existence of the error in $\vec{v}_d$ and $\Delta\theta$. The performance of the two classifiers was degraded in three $\vec{v}_d$s. Therefore, an accurate measurement of $\vec{v}_d$ and $\Delta\theta$ are required for the scenario-based construction method for the successful recognition of targets.

Due to the rotational invariance, Pcs derived by PMC with $B = 200\,\text{MHz}$ were higher than those by PCA + NNC regardless of the error in $\vec{v}_d$ and $\Delta\theta$. However, Pcs of PMC reduced much more than those of PCA + NNC because of the error in estimating COM. Therefore, sufficient $B \geq 200\,\text{MHz}$ is required for PMC to be used for the recognition of the real target. The high resolution technique MUSIC was useful for small Bs; Pcs at $B = 100\,\text{MHz}$ were improved considerably. However, at the sufficient B, the original range-Doppler method was sufficient for the recognition; Pcs at $B = 200\,\text{MHz}$ were not much improved by MUSIC. For the flight scenario with $\vec{v}_d = [0\ -1\ 0]$, a sufficient number of training images are required because Pcs are very sensitive to the reduction of the training data. However, when the target is moving at an angle to a viewing vector ($\vec{v}_d = [-1\ -1\ 0]$ and $\vec{v}_d = [-1\ 0\ 0]$), Pcs are insensitive to the size of the training database and the size of the training database can be reduced to 21.6% of the original size.

ACKNOWLEDGMENT

Sang-Hong Park was with Department of Electrical Engineering at POSTECH, and now he is with Department of Electronic Engineering, Pukyong National University, Busan, Korea. This work was supported by the Brain Korea 21 Project in 2012. This research was supported by Basic Science Research Program through the National Research Foundation of Korea (NRF) funded by the Ministry of Education, Science and Technology (2012002047).

REFERENCES

1. Chen, C. C. and H. C. Andrews, "Target-motion-induced radar imaging," *IEEE Trans. on Aerosp. Electron. Syst.*, Vol. 16, No. 1, 2–14, Jan. 1980.
2. Park, S. H., K. K. Park, J. H. Jung, H. T. Kim, and K. T. Kim, "ISAR imaging of multiple targets using edge detection and hough transform," *Journal of Electromagnetic Waves Applications*, Vol. 22, Nos. 2–3, 365–373, 2008.
3. Park, S. H., K. K. Park, J. H. Jung, H. T. Kim, and K. T. Kim, "Construction of training database based on high frequency RCS prediction methods for ATR," *Journal of Electromagnetic Waves Applications*, Vol. 22, Nos. 5–6, 693–703, 2008.
4. Ma, C.-Z., T. S. Yeo, H. S. Tan, and G. Lu, "Interferometric ISAR imaging on squint model," *Progress In Electromagnetics Research Letters*, Vol. 2, 125–133, 2008.
5. Park, J.-I. and K.-T. Kim, "A comparative study on ISAR imaging algorithms for radar target identification," *Progress In Electromagnetics Research*, Vol. 108, 155–175, 2010.
6. Choi, G. G., S. H. Park, H. T. Kim, and K. T. Kim, "ISAR Imaging of multiple targets based on particle swarm optimization and hough transform," *Journal of Electromagnetic Waves Applications*, Vol. 23, Nos. 14–15, 1825–1834, 2009.
7. Park, S.-H., H.-T. Kim, and K.-T. Kim, "Stepped-frequency ISAR motion compensation using particle swarm optimization with an island model," *Progress In Electromagnetics Research*, Vol. 85, 25–37. 2008.
8. Park, S. H., K. K. Park, J. H. Jung, K. T. Kim, and H. T. Kim, "ISAR imaging of multiple targets using edge detection and hough transform," *Journal of Electromagnetic Waves Applications*, Vol. 22, Nos. 2–3, 365–373, 2008.
9. Park, H.-G., H.-T. Kim, and K.-T. Kim, "Beam tracing for fast RCS prediction of electrically large targets," *Progress In Electromagnetics Research M*, Vol. 20, 29–42, 2011.
10. Park, H.-G., K.-K. Park, H.-T. Kim, and K.-T. Kim, "Improvement of RCS prediction using modified angular division algorithm," *Progress In Electromagnetics Research*, Vol. 123, 105–121, 2012.
11. Chin, H., J.-H. Yeom, H.-T. Kim, and K.-T. Kim, "Improvement of iterative physical optics using previous information to guide initial guess," *Progress In Electromagnetics Research*, Vol. 124, 473–486, 2012.

12. Park, K.-K. and H.-T. Kim, "RCS prediction acceleration and reduction of table size for the angular division algorithm," *Journal of Electromagnetic Waves and Applications*, Vol. 23, Nos. 11–12, 1657–1664, 2012.
13. Kim, B.-C., K.-K. Park, and H.-T. Kim, "Efficient RCS prediction method using angular division algorithm," *Journal of Electromagnetic Waves and Applications*, Vol. 23, No. 1, 65–74, 2009.
14. Garcia-Donoro, D., I. Martinez-Fernandez, L. E. Garcia-Castillo, Y. Zhang, and T. K. Sarkar, "RCS computation using a parallel in-core and out-of-core direct solver," *Progress In Electromagnetics Research*, Vol. 118, 505–525, 2011.
15. De Cos, M. E., Y. Alvarez Lopez, and F. Las-Heras "On the influence of coupling AMC resonances for RCS reduction in the SHF band," *Progress In Electromagnetics Research*, Vol. 117, 103–119, 2011.
16. De Cos, M. E., Y. Alvarez Lopez, and F. Las-Heras, "A novel approach for RCS reduction using a combination of artificial magnetic conductors," *Progress In Electromagnetics Research*, Vol. 107, 147–159, 2010.
17. Gao, P. C., Y. B. Tao, and H. Lin, "RCS prediction using multiresolution shooting and bouncing ray method on the GPU," *Progress In Electromagnetics Research*, Vol. 107, 187–202, 2010.
18. Wang, M.-J., Z.-S. Wu, Y.-L. Li, and G. Zhang, "High resolution range profile identifying simulation of laser radar based on pulse beam scattering characteristics of targets," *Progress In Electromagnetics Research*, Vol. 96, 193–204, 2009.
19. Han, S.-K., H.-T. Kim, S.-H. Park, and K.-T. Kim, "Efficient radar target recognition using a combination of range profile and time-frequency analysis," *Progress In Electromagnetics Research*, Vol. 108, 131–140, 2010.
20. Menon, M. M., E. R. Boudreau, and P. J. Kolodzy, "An automatic ship classification system for ISAR imagery," *The MIT Lincoln Laboratory Journal*, Vol. 6, No. 2, 289–308, 1993.
21. Park, S.-H, M.-G. Joo, and K.-T. Kim, "Construction of ISAR training database for automatic target recognition," *Journal of Electromagnetic Waves Applications*, Vol. 25, Nos. 11–12, 1493–1503, 2011.
22. Li, X., G. Liu, and J. Ni, "Autofocusing of ISAR images based on entropy minimization," *IEEE Trans. on Aerosp. Electron. Syst.*, Vol. 35, No. 4, 1240–1251, Oct. 1999.

23. Wang, J., X. Liu, and Z. Zhou, "Minimum-entropy phase adjustment for ISAR," *IEE Proc. of Radar, Sonar and Nav.*, Vol. 151, No. 4, 203–209, Aug. 2004.
24. Park, S.-H., H.-T. Kim, and K.-T. Kim, "Enhanced range alignment using a combination of a polynomial and Gaussian basis functions," *Progress In Electromagnetics Research*, Vol. 95, 381–396, 2009.
25. Huang, C.-W. and K.-C. Lee, "Application of ICA technique to PCA based radar target recognition," *Progress In Electromagnetics Research*, Vol. 105, 157–170, 2010.
26. Lee, K.-C., J.-S. Ou, and M.-C. Fang, "Application of SVD noise-reduction technique to PCA based radar target recognition," *Progress In Electromagnetics Research*, Vol. 81, 447–459, 2008.
27. Duda, R. O., P. E. Hart, and D. G. Stork, *Pattern Classification*, 2nd Edition, Wiley, New York, 2001.
28. Kim, K.-T., D.-K. Seo, and H.-T. Kim, "Classification of ISAR images," *IEEE Trans. on Antennas and Propag.*, Vol. 53, No. 5, 1611–1621, May 2005.
29. Lim, H. and N.-H. Myung, "A novel hybrid AIPO-MoM technique for jet engine modulation analysis," *Progress In Electromagnetics Research*, Vol. 104, 85–97, 2010.
30. Lim, H., J. H. Yoo, C. H. Kim, K. I. Kwon, and N. H. Myung, "Radar cross section measurements of a realistic jet engine structure with rotating parts," *Journal of Electromagnetic Waves and Applications*, Vol. 25, No. 7, 999–1008, 2010.
31. Lim, H. and N.-H. Myung, "High resolution range profile-jet engine modulation analysis of aircraft models," *Journal of Electromagnetic Waves and Applications*, Vol. 25, Nos. 8–9, 1092–1102, 2011.
32. Park, J.-H., H. Lim, and N.-H. Myung, "Modified Hilbert-Huang transform and its application to measured micro doppler signatures from realistic jet engine models," *Progress In Electromagnetics Research*, Vol. 126, 255–268, 2012.